Surface & Coatings Technology 205 (2011) 2964–2969

Contents lists available at ScienceDirect

Surface & Coatings Technology

journal homepage: www.elsevier.com/locate/surfcoat

Finite element simulation of tensile bond strength of atmospheric plasma spraying thermal barrier coatings

Shen Wei, Wang Fu-chi, Fan Qun-bo *, Ma Zhuang, Yang Xue-wen

School of Materials Science and Engineering, Beijing Institute of Technology, Beijing 100081, PR China

ARTICLE INFO

Article history:
Received 25 June 2010
Accepted in revised form 1 November 2010
Available online 5 November 2010

Keywords:
Coatings
Modified Brazilian disc
FEM
Tensile bond strength

ABSTRACT

Before thermal cycling or thermal exposure, tensile failure of atmospheric plasma spraying (APS) thermal barrier coatings (TBCs) usually occurs by spallation of the ceramic coating at or near the bond coating, due to the accumulation of microcracks damage. In the current paper, finite element geometric models based on the real microstructural image of TBCs are generated, and the microcracks growth induced by the uniaxial tensile loading is simulated by employing LS-DYNA code with a failure criterion determined by maximum tensile stress of yttria partially stabilized zirconia (YSZ). Additionally, the modified Brazilian disc specimens with a central hole are used to obtain the intrinsic static failure criterion of non-defective YSZ. By means of a statistical method in conjunction with finite element method (FEM) results, the tensile bond strength of APS TBCs is calculated as 40 MPa in this paper. Meanwhile, damage accumulation and microcrack growth can be observed vividly by simulation processing. The numerical simulation result agrees well with the corresponding experimental result. It is shown that the methodology developed in this paper is very efficient in understanding damage evolution in TBCs.

1. Introduction

Atmospheric plasma spraying (APS) is a low-cost method for depositing ceramic thermal barrier coatings (TBCs) used to operate in the demanding high-temperature environment of aircraft engines, such as combustors, fuel vaporizers, after-burner flame holders, and turbine vanes [1]. APS TBCs comprise metal and ceramic multilayers: ceramic layer, normally yttria stabilized zirconia (YSZ), is used as a top coat (TC); while metal layer used as bond coat (BC) is typically made of a NiCrAlY or NiCoCrAlY alloy. TC acts as the thermal insulator while BC provides adherence for the ceramic outer layer. The tensile bond strength or adhesion strength of TBCs is an important parameter in failure, depending significantly on the coatings' heterogeneous morphology due to a complex microstructure of particles with voids and microcracks in irregular shapes and distributions.

The bond strength of TBCs has been studied experimentally and theoretically [2–8]. Measurement and analysis of adhesion strength for thermally sprayed coatings have been discussed and summarized well by C.K. Lin and C.C. Benrndt [9]. However, up to now, the microcracks initiation and propagation based on realistic microstructure were not taken into account. In this context, we present a methodology to generate a finite element grid model based on the realistic microstructure of TBCs. Additionally, a novel method is proposed to test the failure criterion of YSZ. Meanwhile, with the aid of finite element program, the tensile bond strength of APS TBCs is successfully obtained by modeling the microcracks growth by increasing the external tensile stress.

2. Finite element model based on the microstructure of TBCs

One of the most novel methods of building finite element model by capturing accurately real microstructures was developed by Edwin Fuller and co-workers at the National Institute of Standards and Technology (NIST) in the form of a package that is termed as “OOF” (Object Oriented Finite Element Analysis) [10]. Similarly, in our research, to better capture TC/BC interfaces morphology, digital image processing technique combined with finite element method is also employed to build two-dimensional (2D) finite element models based on the real characteristics of TC and BC microstructures. First, sample preparation is performed with a cold-setting resin with vacuum impregnation for 30 min, then polished by SiC papers from #200 to #2000 and diamond paste from 3 μm to 1 μm. At last, scanning electron microscopy (SEM) is used to obtain images at ×350. The procedure adopted for image acquisition entails a back-scattered electron imaging mode for higher contrast between defects and ceramic matrix. These SEM images are then used for image analysis.

An image may be defined as 2D function $f(x,y)$, where x and y are plane coordinates, and the amplitude of f at any pair of coordinates (x,y) is the gray level of the image at that point. When x,y and f are all finite and discrete quantities, the image is a gray scale digital image, and any image can be transferred to a gray scale image.

Suppose one microstructural image of TBCs corresponds to $f(x,y)$, in such a way that all materials involved in an image have gray levels

* Corresponding author.
E-mail address: fanqunbo@bit.edu.cn (F. Qun-bo).

0257-8972/$ – see front matter © 2010 Elsevier B.V. All rights reserved.
doi:10.1016/j.surfcoat.2010.11.003

grouped into n modes. One obvious way to extract one from the others is to select the thresholding value T that separates these modes. Then, any point (x,y) for which $f(x,y) \in [T_{i-1}, T_i]$ is assigned with an appointed material label, where i is the material index number.

Essentially, a digital image is a collection of pixels, and a finite element model is a collection of finite elements. With one pixel corresponding to one finite element, the collection of pixels can be transferred to a collection of finite elements [11]. As mentioned previously, different gray level ranges reflect different materials. In this way, the finite element grid model shown in Fig. 1(b) based on realistic microstructures of APS TBCs in Fig. 1(a) with the size of 356 $\mu m \times 267$ μm is generated by thresholding segmentation and finite element mesh generation principle. Considering that the numerical simulation of microcracks growth with the finite element method is sensitive to the employed mesh, more than 60,000 square elements are built in finite element models. Belytschko and co-workers' [12–14] researches show that only if the finite element is small enough we can get a reasonable approximation to simulate the stress intensity in microcracks tip. Supposing a crack with specified size distribution, orientation direction and morphology in the finite element model with dimensions 356 μm × 267 μm according with the size of Fig. 1(a), it is found that when the element size near crack tip is less than 1.8 μm × 1.8 μm, there is no significant change in stress concentration near the crack tip. Hence, in the current study, the element size of only 1 μm × 1 μm is acceptable. Obviously, the defects and the interface shapes between TC and BC using this method are closer to the realistic conditions. Incidentally, due to the limited resolution of micrograph, some very thin microcracks and small pores not shown in these images cannot be taken into account in our models, and they are ignored in our simulation for their limited influence on microcracks growth.

Actually, the tensile bond strength of TBCs corresponds to the three-dimensional (3D) case in nature. However, it is hard to construct the actual three-dimensional (3D) model of TBCs accurately. Recently, 3D microstructure models based on 2D images by novel methodologies were proposed by some scholars [15–17]. However, there is no guarantee that the 3D model captures completely the same structure as the original coating, not to mention the high computation cost. Noticeably, a large number of random 2D finite element simulations can effectively reduce the influence of the third dimension in the tensile deformation analysis. Therefore, it is assumed that enough 2D results could reflect the inherent tensile bond strength of TBCs closely in the current study.

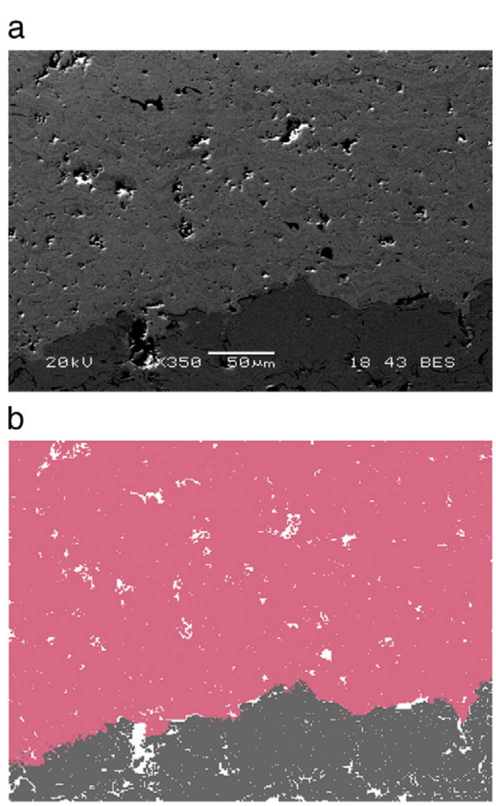

Fig. 1. (a) The cross-section microstructure of APS TBCs. (b) The finite element grid model of APS TBCs with more than 60,000 elements.

3. External load, boundary conditions and material properties

Numerical simulation is performed with 2D geometric model using LS-DYNA code to model the microcrack growth of the TBCs during the uniaxial tensile loading. Plane strain elements are used in finite element model. As the residual stresses induced by the plasma spraying of the TBC are known to be on the order of 3–5 MPa [18,19], the TBCs are considered to be stress-free at the beginning of tensile test. To obtain the tensile strength of TBCs along the spray direction, a changing stress condition is prescribed on both the top and bottom boundaries. One boundary is subjected to quasi-static normal stress σ, as shown in Fig. 2, and the other is fixed. In our simulation, the brittle material behavior of YSZ in Table 1 is defined as elasticity with a failure condition determined by the maximum tensile stress. And the elastic-plastic model is chosen to model NiCoCrAlY (BC material) in Table 1. During the simulation, the element satisfied with failure criterion will be deleted timely from the model, so the microcrack growth of TBCs is observable.

4. Failure criterion of YSZ by the modified Brazilian disk

To simulate the cracking process of the model like Fig. 1(b), the failure criterion of the materials is necessary, especially for the brittle ceramic materials. In our simulation, the maximum tensile stress is defined as the failure criterion of YSZ. An appropriate experimental method shall be employed correspondingly.

The uniaxial compression Brazilian test is generally employed to acquire the tensile strength of the brittle materials indirectly. Jeong and co-workers [20] presented a modified Brazilian disk (MBD) specimen to acquire the indirect tensile strength of 'Lead Crystal Glass' material. In the present research, the MBD specimen with one small hole in the center of the specimen, shown in Fig. 3(a), which contributes to the stress concentration field around the hole, is utilized to obtain the tensile strength of YSZ due to the presence of high tensile stress concentration at notch tip (Fig. 4). For such specimen, the strength of material can be described as:

$$\sigma_{max} = \alpha \cdot \frac{3P(R_1 + R_2)}{\pi \cdot h(R_1 - R_2)^2} \tag{1}$$

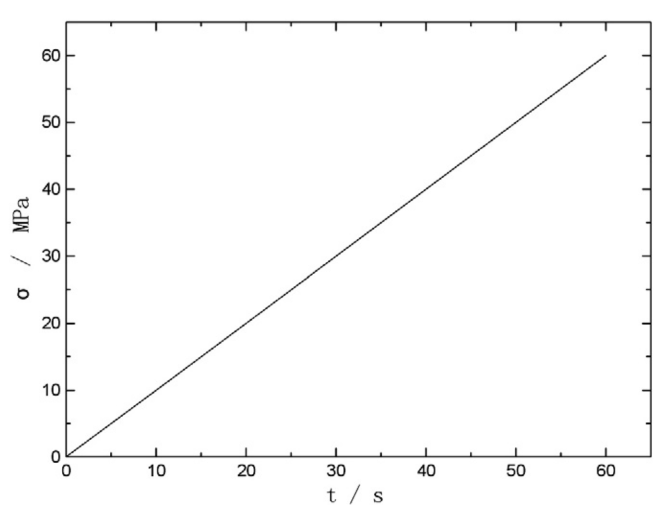

Fig. 2. The external tensile stress versus time.

Table 1
Material properties used in the model.

	Young's modulus	Poisson ratio	Yield stress	Failure stress
	E (GPa)	υ(-)	σ_y (MPa)	σ_f (MPa)
YSZ	80	0.26	–	215
NiCoCrAlY	200	0.3	426	–

where $\sigma_{\max}$, P and h are the tensile strength of material, the maximum applied loading and the thickness of MBD specimen. α is the stress concentration factor, which is determined by the ratio of inner radius R_2 and outer radius R_1.

Cylindrical disks are prepared by uniaxial pressing ($P=30$ MPa) of YSZ powders (40–60 nm spheres) followed by isostatic pressing ($P=200$ MPa) at room temperature. Subsequently, MBD specimens are generated by drilling a hole in the center of disks and sintering at 1350 °C for 5 h. Density (ρ) of the specimens was measured as 96.8% using the Archimedes principle, with deionized water as the immersion medium. Einarsrud and co-workers' [21] research showed that there is no significant change in mechanical properties for YSZ with dense materials (≥96%). Meanwhile, the grain sizes of MBD specimens ranging in hundreds of nanometers are close to the grain sizes of coatings (70–100 nm [22]). Therefore, the prepared dense bulk YSZ in this paper can be regarded as non-defective material, whose fracture stress reflects the intrinsic failure criterion of YSZ. By employing the uni-axial compression Brazilian test in conjunction with Eq. (1), the static fracture stress of our specimens is found to be 215 MPa under the quasi-static loading, an average of 10 measurements. In Fig. 3(b), YSZ specimen has been split into two pieces since the high tensile stress concentration at notch reaches the static fracture stress. It has been observed that all specimens have been split near the hole in the center of MBD specimens under static loadings, a nice agreement with Brazilian test conditions.

It might be noted that splat interfaces in the coatings cannot be generated in finite element models because the interface properties are not very clear as yet [23]. Fortunately, the splat interfaces are usually not the most vulnerable part in YSZ coating during tensile processing. Accordingly, the failure criterion of YSZ could be used to model the microcracks growth. Here, the YSZ and splat interfaces are considered as one material, but the effects of the splat interfaces on the effective modulus are taken into account. In our previous study [24], new expression for effects of splat interfaces on the effective Young's modulus has been proposed as follows

$$E_{eff} = E_0 \cdot \frac{1}{1+\beta} \tag{2}$$

where, β is the Young's modulus effect coefficient of splat interfaces, E_{eff} is the effective Young's modulus, and E_0 is Young's modulus of the bulk material with the value of 200 GPa [23]. For the nano-structured

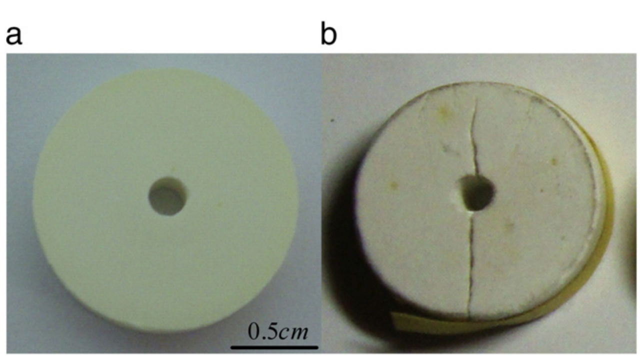

Fig. 3. (a) The MBD specimen of YSZ. (b) Quasi-static fracture phenomena of MBD specimen.

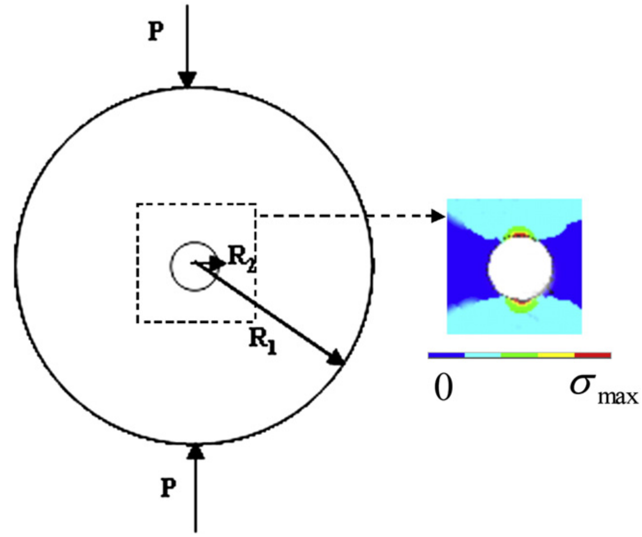

Fig. 4. Schematic illustration of MBD test with maximum tensile stress distribution near the hole.

YSZ coatings prepared with the basic operating parameters listed in Table 2, β can be chosen as 1.5. Thus, the Young's modulus of YSZ containing interfaces is expressed as

$$E_{eff} = 0.4 \cdot E_0 = 80GPa \tag{3}$$

We assume that the splat interfaces are well-proportionally distributed mainly in parallel with the interface, ignoring the localized effects in YSZ caused by splat interfaces.

5. Results and discussion

In this section, the model of damage initiation and growth, and fracture in TBCs with real structure is presented. In the presence of a tensile loading, the crack generated during spraying will have the largest stress intensity factor and propagate first. The local stress field at the initial cracking stage is shown in Fig. 5(a), where the tensile stress concentrates on the tip of the transverse crack in region A. It is reasonable to expect that high tensile stresses that arise in region A will facilitate the crack propagation when the tensile loading is increasing. Fig. 5(b) and (c) show the cracking process at 33.2 s and 33.6 s, respectively. After the crack initiates in region A, it propagates along the TC/BC interface at first. And then the irregular geometry of the interface alters the propagation direction of cracks, thus preventing further fracture along the TC/BC interface, and cracks continue to propagate in TC. Comparing Fig. 5(d) shows that the final damage evolution is obvious at 34 s. Sometimes, fracture even occurs in TC away from the interface, as shown in Fig. 6. The long transverse cracks in TC at or near TC/BC interface are found to be the most vulnerable parts of APS TBCs.

When loads are gradually applied to a solid body, they will lead to the deformation of the material. Provided no energy is lost in the form of heat, the external work done by the loads will be converted into

Table 2
Basic operating parameters of plasma spraying.

	Primary gas	Second gas	Carrier gas	Electric current	Spraying distance	Spraying thickness
	scf/h	scf/h	scf/h	(A)	mm	mm
Top coating	75	45	8	850	75	0.3
Bond coating	120	20	10	700	75	0.1

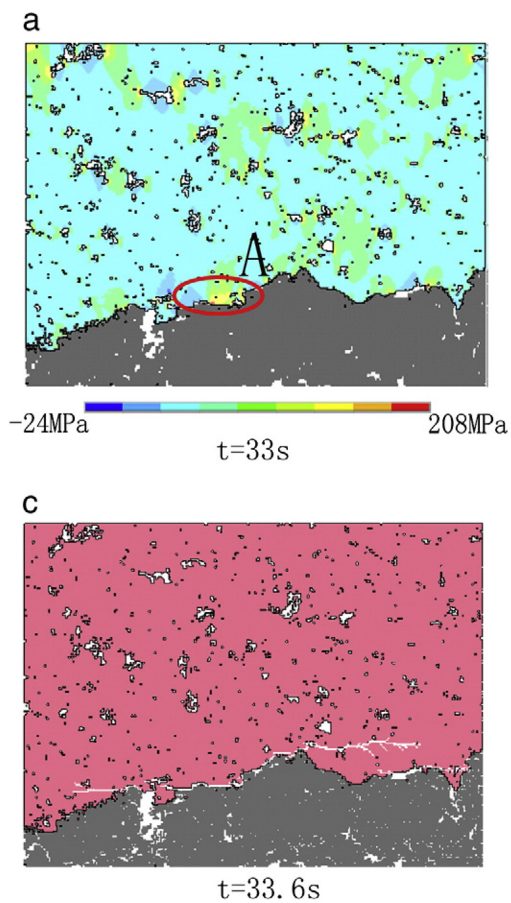

Fig. 5. (a) Maximum tensile stress distribution in the beginning of crack growth. (b) Cracks growth at 33.2 s. (c) Cracks growth at 33.6 s. (d) Fracture at 34 s.

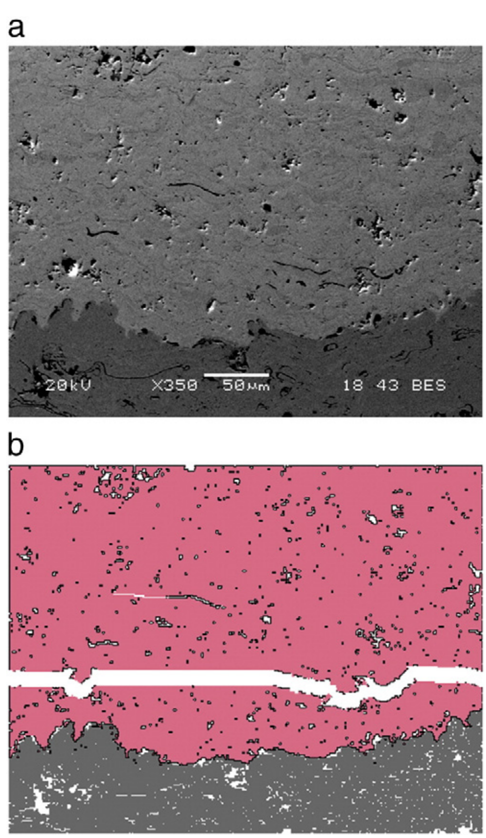

Fig. 6. (a) The cross-section microstructure of APS TBCs. (b) Simulation results of fracture.

internal work called strain energy. When loads are gradually applied to TBCs, the strain energy goes up correspondingly. With increasing the load, the stress intensity at the crack tip rises until a threshold value and the crack grows uncontrollably. Meanwhile, a large number of elements satisfied with failure criterion are deleted from the model, and thus, the strain energy releases quickly. As presented in Fig. 7, the external load at the time 33 s corresponding to the peak of the strain energy curves is chosen as the tensile bond strength of APS TBCs in Fig. 1. About 60 random SEM images from 6 different specimens are taken into account, and simulation results show a tensile cohesive failure within the top coating with values ranging from 28 to 50 MPa.

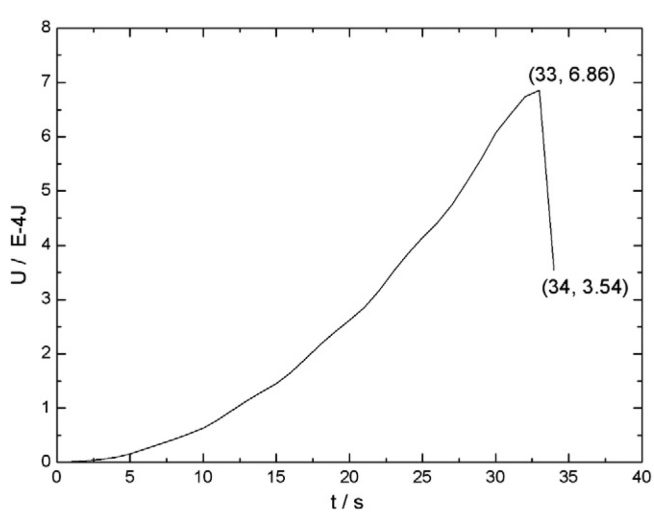

Fig. 7. Strain energy changing with time.

The tensile bond strength is a stochastic parameter that requires a statistical treatment. It is found that the tensile bond strength has a characteristic scatter around a certain mean value. To evaluate this characteristic behavior, Weibull [25] has described a statistical distribution function of fracture events. A modified formula of Weibull distribution probability paper method is given as follows

$$ln\ ln\left(\frac{1}{1-P_i}\right) = m(\ ln\sigma_i - \ ln\sigma_0) \tag{4}$$

where P_i is the fraction of the total number of microstructures that will fracture under the applied stress distribution σ_i. The exponent m is known as the Weibull modulus, which expresses the statistical scatter of fracture events. A high Weibull modulus indicates a low scatter. σ_0 is the tensile bond strength by Weibull analysis. For a serials of simulation bond strengths of TBCs, $\sigma_{(1)},\ldots\ \sigma_{(n)}$, they are obtained by ordering $\sigma_{(i)}$ from the smallest to the largest to get $\sigma_1 \le \cdots \sigma_i \le \cdots \le \sigma_n$ and then associated with $P_i = (i-0.5)/n$. Thus $ln\ ln\left(\frac{1}{1-P_i}\right)$against $\ln \sigma_i$ can be fitted as a line by the least squares estimates of (P_i,σ_i), shown in Fig. 8. Since $\ln \sigma_i = 3.68$ yields $ln\ ln\left(\frac{1}{1-P_i}\right) = 0$, we can read off an estimate for $\sigma_0 = 40MPa$ from the abscissa scale where the fitted line intercepts the ordinate level 3.68.

Following the procedure given in ASTM-C633-79 standard, 20 specimens are prepared except that the length of the samples is increased from 25.4 mm to 38.1 mm, thus reducing the effect of epoxy adhesive used (see more discussion in [26]). The surface of uncoated specimens was grit blasted to enhance the adhesion strength. A tensile load rate of 500 N/s is applied to these specimens. Experimental results show a tensile cohesive failure within the top coating with values ranging from 29 to 43 MPa.

Similarly, Weibull distribution probability paper method is used to statistically treat the experimental data of tensile bond strength, as shown in Fig. 9. Since $\ln \sigma_i = 3.58$ yields $ln\ ln\left(\frac{1}{1-P_i}\right) = 0$, we can read off an estimate for$\sigma_0 = 37MPa$. A comparison between experimental results and numerical results shows a good agreement. Therefore, the methodology developed in our present work is reliable to predict the tensile bond strength of TBCs.

6. Conclusions

(1) Finite element mesh generation principle combined with digital image processing approach has been used to generate the finite element grid model based on the realistic microstructural images of TBCs.

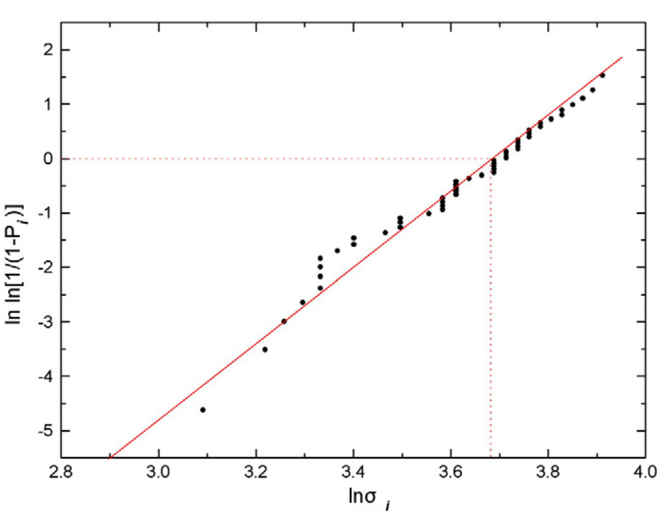

Fig. 8. Weibull distribution of tensile bond strengths from simulation results of APS TBCs.

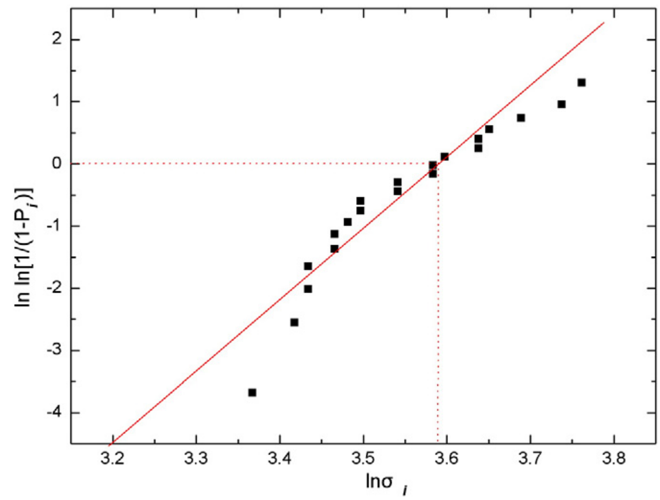

Fig. 9. Weibull distribution of tensile bond strengths from experimental results of APS TBCs.

(2) The modified Brazilian disc specimens with a central hole by conventional sintering technology are used to obtain the failure criterion of non-defective bulk material of yttria partially stabilized zirconia (YSZ). The fracture tensile stress of dense YSZ is found to be 215 MPa under the quasi-static tensile loading.

(3) With a failure condition determined by the maximum tensile stress, LS-DYNA code is employed to model microcracks growth of APS TBCs during the tensile process, and the long transverse cracks in TC at or near TC/BC interface are found to be the most vulnerable parts of APS TBCs.

(4) By means of Weibull analysis, the tensile bond strengths of simulation results and experimental results are found to be 40 MPa and 37 MPa, respectively. The numerical simulation result agrees well with the corresponding experimental result. The methodology presented in this paper is found to be effective to predict the tensile bond strength of coating.

Acknowledgment

We acknowledge the funding supports of the project (No. 50801005) from the Chinese National Nature Science Foundation.

References

[1] N.P. Padture, M. Gell, E.H. Jordan, Science 296 (2002) 280.
[2] M. Andritschky, V. Teixeira, L. Rebouta, H.P. Buchkremer, StD. , Surf. Coat. Technol. 76-77 (1995) 101.
[3] M. Gell, J. Eric, V. Krishnakumar, K. McCarron, B. Barber, Y.H. Sohn, V.K. Tolpygo, Surf. Coat. Technol. 120-121 (1999) 53.
[4] T.Y. Cho, J.H. Yoon, J.Y. Cho, Y.K. Joo, J.H. Kang, S. Zhang, H.G. Chun, S.Y. Hwang, S.C. Kwon, Surf. Coat. Technol. 203 (2009) 3250.
[5] A.K. Ray, N. Roy, A. Kar, A.K. Ray, S.C. Bose, G. Das, J.K. Sahu, D.K. Das, B. Venkataraman, S.V. Joshi, Mater. Sci. Eng. A 505 (2009) 96.
[6] N.Y. Cao, Y. Kagawa, Y.F. Liu, Surf. Coat. Technol. 202 (2008) 3413.
[7] N.Y. Cao, Y.F. Liu, Y. Kagawa, Surf. Coat. Technol. 202 (2008) 3109.
[8] J. Yan, A.M. Karlsson, M. Bartsch, X. Chen, Comput. Mater. Sci. 44 (2009) 1178.
[9] C.K. Lin, C.C. Benrndt, J. Therm. Spray Technol. 3 (1) (1994) 75.
[10] S.A. Langer, W.C. Carter, E.R. Fuller Jr., Object Oriented Finite Element Analysis for Materials Science, Center for Theoretical and computational Materials Science and the Information Lab. at the NIST, 1997, URL: www.ctcms.nist.gov/oof/
[11] S. Wei, F. Qun-bo, W. Fu-chi, M. Zhuang, Comput. Mater. Sci. 46 (2009) 600.
[12] T. Belytschko, T. Black, Int. J. Numer. Methods Eng. 45 (1999) 601.
[13] N. Moes, J. Dolbow, T. Belytschko, Int. J. Numer. Methods Eng. 46 (1999) 131.
[14] M. Stolarska, D.L. Choop, N. Moes, T. Belytschko, Int. J. Numer. Methods Eng. 51 (2001) 943.
[15] K. Terada, T. Miura, N. Kikuchi, Comput. Mech. 20 (1997) 331.
[16] N. Lippmann, Th. Steinkopff, S. Schmauder, P. Gumbsch, Comput. Mater. Sci. 9 (1997) 28.
[17] A.P. Roberts, E.J. Garboczi, J. Am. Ceram. Soc. 83 (12) (2000) 3041.
[18] A.M. Freborg, B.L. Ferguson, W.J. Brindley, G.J. Petrus, Mater. Sci. Eng. A 245 (1998) 182.

[19] E.P. Busso, J. Lin, S. Sakurai, M. Nakayama, Acta Mater. 49 (2001) 1515.
[20] J. Jeong, H. Adib, G. Pluvinage, J. NonCryst. Solids 351 (2005) 2065.
[21] P. Dahl, I. Kaus, Z. Zhao, M. Johnsson, M. Nygren, K. Wiik, T. Grande, M. Einarsrud, Ceram. Int. 33 (2007) 1603.
[22] C. Zhou, N. Wang, Z. Wang, S. Gong, H. Xu, Scr. Mater. 51 (2004) 945.
[23] Z. Wang, A. Kulkarni, S. Deshpande, T. Nakamura, H. Herman, Acta Mater. 51 (2003) 5319.
[24] S. Wei, W. Fu-chi, F. Qun-bo, H. Dan, M. Zhuang, Surf. Coat. Technol. 204 (2010) 3376.
[25] W. Weibull, J. Appl. Mech. 18 (1951) 293, Stockholm, Sweden.
[26] W. Han, E.F. Rybicki, J.R. Shadley, J. Therm. Spray Technol. 2 (2) (1993) 145.